

Article

Selective Hydrogenation of Adiponitrile to 6-Aminocapronitrile over Ni/ α -Al₂O₃ Catalysts Doped with K₂O and La₂O₃

Lei Zhao ^{1,2}, Caiyun Wang ², Jixiang Chen ², Ziyang Nie ², Jiyan Zhang ² and Xuebin Lu ^{3,*}¹ Tianjin Academy of Environmental Sciences, Tianjin 300191, China; zhaoeca@126.com² Department of Catalysis Science and Engineering, School of Chemical Engineering and Technology, Tianjin University, Tianjin 300072, China; 18840888935@163.com (C.W.); jxchen@tju.edu.cn (J.C.); zhangj_581@163.com (Z.N.); jy Zhang@tju.edu.cn (J.Z.)³ School of Science, Tibet University, Lhasa 850000, China

* Correspondence: xbltju@tju.edu.cn

Abstract: A series of Ni/Al₂O₃, Ni/K₂O-Al₂O₃ and Ni/La₂O₃-K₂O-Al₂O₃ catalysts that possess high activities for partial hydrogenation of adiponitrile to 6-aminocapronitrile has been successfully synthesized by the impregnation method. The catalytic performance was investigated under atmospheric pressure and in the absence of ammonia and a significant enhancement in the activity after the introduction of potassium oxide and lanthana was observed. Aiming to study the influence of K₂O and La₂O₃ promoters on the physicochemical properties, we characterized the catalysts by N₂ adsorption/desorption, XRD, H₂-TPR, H₂-chemisorption, H₂-TPD and TEM techniques. A combination of XRD, TEM and H₂-chemisorption showed that Ni⁰ particles with a higher dispersion are obtained after the addition of La₂O₃. Compared with the Ni/Al₂O₃ catalyst, the Ni/La₂O₃-K₂O-Al₂O₃ catalyst with an appropriate amount of promoter enjoys a more catalyst surface alkalescence, enhances the electronic density of nickel and higher dispersion of nickel and exhibits higher activity and 6-aminocapronitrile selectivity than Ni/ α -Al₂O₃ during the hydrogenation of adiponitrile in the absence of ammonia, i.e., K₂O and La₂O₃ improved the performance of the nickel-based catalyst.

Keywords: 6-aminocapronitrile; partial hydrogenation; electronic density

Citation: Zhao, L.; Wang, C.; Chen, J.; Nie, Z.; Zhang, J.; Lu, X. Selective Hydrogenation of Adiponitrile to 6-Aminocapronitrile over Ni/ α -Al₂O₃ Catalysts Doped with K₂O and La₂O₃. *Catalysts* **2023**, *13*, 934. <https://doi.org/10.3390/catal13060934>

Academic Editor: Leonarda Liotta

Received: 9 April 2023

Revised: 10 May 2023

Accepted: 12 May 2023

Published: 25 May 2023



Copyright: © 2023 by the authors. Licensee MDPI, Basel, Switzerland. This article is an open access article distributed under the terms and conditions of the Creative Commons Attribution (CC BY) license (<https://creativecommons.org/licenses/by/4.0/>).

1. Introduction

Aminonitriles are a class of important chemicals that have a variety of industrial applications. For example, aminonitriles can be used as monomers for producing high molecular weight polyamides. In particular, 6-aminocapronitrile (ACN) is the key intermediate in a new route for synthesis of caprolactam (CPL) [1] for the fabrication of nylon-6 [2,3]. Given the continuing expansion of the polyamide market, the need for CPL is constantly growing.

Traditionally, CPL is mainly produced from cyclohexanone, a process that generates 4.5 kg of ammonium sulfate per kg of CPL produced. Alternatively, the route of hydrocyanation of butadiene is a novel salt-free process to obtain CPL at a lower cost than is needed for the current process, and it is comprised of three courses, i.e., hydrocyanation of butadiene to adiponitrile (ADN), partial hydrogenation of ADN to ACN and the hydrolysis cyclization of ACN to CPL. The key step of this new process is the partial hydrogenation of ADN to ACN, and the challenge is to stop the reaction halfway to avoid deep hydrogenation to 1,6-hexanediamine (HMDA). Compared with the current ketone-hydroxylamine processes, the novel route has some advantages, such as a lower cost, less environmental pollution and the absence of ammonium sulfate [4]. This minimizes waste, one of the criteria of green chemistry for the manufacturing and application of chemical products [5].

In industry, the hydrogenation of ADN is performed in a liquid phase at a high pressure, in which the Raney Ni is probably the most frequently used catalyst [6–10]. Raney Ni is very active, but it has a low mechanical resistance, is pyrophoric and is difficult to completely remove from the process fluid. Meanwhile, a large amount of ammonia

or other alkaline hydrate is necessary to decrease side reactions leading to secondary and tertiary amines, presumably due to the presence of diamine intermediate. These condensation compounds can also remain on the metallic surface and block the catalytic active sites [11]. Therefore, a great number of attempts have been made to replace Raney Ni with catalysts with a cleaner preparation, which are more resistant and more selective supported [12–19], or unsupported [20–23] catalysts, over which the ADN hydrogenation could be performed under mild conditions [24]. Other precursors, such as hydrotalcites of Ni/Mg/Al, allow variation in the MgO/Al₂O₃ ratio and thus allow control of the acidity of the final catalysts [25]; when this ratio increases, the selectivity to primary amines increases for the hydrogenation of ADN. From these selected examples, it comes out that Ni-based materials are excellent candidates for preparing active and selective catalysts. Nevertheless, some questions still exist in the partial hydrogenation of ADN, such as difficulty in achieving high ACN selectivity and ADN conversion simultaneously and the catalyst being able to be deactivated easily; meanwhile, the regeneration of the catalyst after use has been seldom dealt with.

When the activity and selectivity of a reaction depends on the size of the metal particles, the reaction is called “structure sensitive” and in this case, the choice of proper preparation methods becomes of primary importance to obtain the best catalyst performance [26]. F. Medina et al. [21] think that the hydrogenation of adiponitrile gives selectively to the primary amines as a structure-sensitive reaction, and S. Alini et al. [19] also find that the Rh/Al₂O₃ catalyst, prepared with precipitation via urea decomposition and is reduced using the liquid phase route, gives a lower conversion and lower selectivity than the catalyst obtained by the ion exchange technique and is reduced in the same way in ADN hydrogenation. This would suggest a certain “structure sensitivity” of the reaction studied, and this idea was enforced by the fact that very low performance in this reaction was showed by an Rh/Al₂O₃ catalyst prepared by wet impregnation with a mean Rh crystallite size of 20 nm.

As we all know, lanthana usually acted as a textural promoter, which can improve the dispersion of Ni particle crystallites and further increase the hydrogen adsorption capacity of the catalysts [27]; on the other hand, it is reported that the addition of potassium oxide in small amounts could enhance ACN selectivity over nickel catalysts [13,15,21]. In this work, an attempt was made to prepare a novel nickel catalyst co-promoted with potassium oxide and lanthana for the partial hydrogenation ADN to ACN at atmospheric pressure and in the absence of ammonia, in order to find a catalyst with better catalytic performance for ADN hydrogenation, and furthermore, to validate the “structure sensitivity” of the partial hydrogenation of ADN to ACN.

2. Results and Discussion

2.1. Catalyst Characterization

2.1.1. Structural and Textural Properties

The effects of K₂O and La₂O₃ on the textural characteristic of the Ni/ α -Al₂O₃ sample were studied by the nitrogen adsorption/desorption technique. Figure 1 shows the N₂ adsorption–desorption isotherms of NA, NKA and NKLA. All samples possessed type IV hysteresis loop isotherms, and the adsorbed quantity at p/p_0 of 0.99 increased in the following sequence: NA, NKA and NKLA. A higher adsorbed quantity indicates larger pore volume.

The surface areas (S_{BET}), pore volumes (V_p) and average pore sizes (D_p) of the catalysts are summarized in Table 1. Obviously, the NKLA sample possessed the highest specific surface area of 18.9 m²·g^{−1} and the largest pore volume of 0.077 cm³·g^{−1}. As a general tendency, the addition of the promoter apparently decreased the S_{BET} value as well as the V_p , which suggested a negative effect of additive on the textural properties. Yet here, very interestingly, with the dope of K₂O, the S_{BET} values decreased and the V_p and D_p increased. While the addition of La₂O₃ significantly increased the S_{BET} and V_p , the D_p had no nearly

change, which might be associated with the positive effect of La on the dispersion of Ni. Yet, all the samples retained the mesopores in the $15.5 < D_p < 17.5$ nm range.

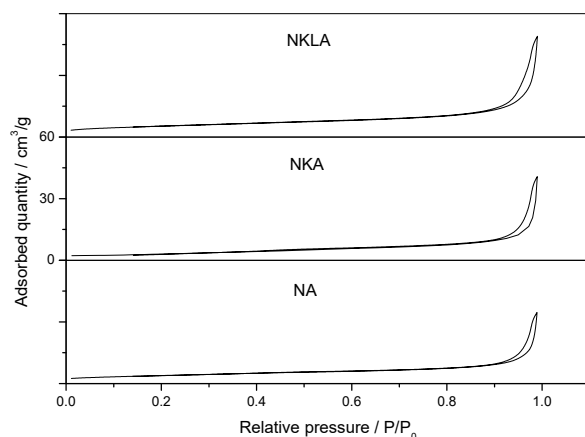


Figure 1. N_2 adsorption–desorption isotherms of NA, NKA and NKLA.

Table 1. Textural properties and H_2 -chemisorption data of NA, NKA and NKLA catalysts.

Catalyst	S_{BET} /m ² /g	V_p /cm ³ /g	D_p /nm	Chemisorbed H_2 /μmol/g.cat
NA	14.0	0.054	15.6	9.4
NKA	10.9	0.063	17.3	12.9
NKLA	18.9	0.077	17.0	53.4

2.1.2. H_2 -TPR

Figure 2 shows H_2 -TPR profiles of all three samples and NiO as a reference. There were two peaks in all of the TPR curves. The reduction peak at around 523 K could be assigned to the reduction of the nickel oxide, and some authors thought that its occurrence or nonoccurrence did not affect the remainder of the TPR profile [28]. The main reduction peak at about 673 K should be attributed to bulk NiO. It is clear that the addition of the promoters increases the initial reduction temperature of the catalysts, suggesting that the interaction between them may elevate the activation energy of the nickel oxide reduction and inhibit its reduction. The hydrogen consumption peaks gradually widen in the following sequence: NA, NKA and NKLA, which indicates that the addition of promoters leads to a better dispersion of the nickel oxide particles, thus improving the reduction rate of the catalyst.

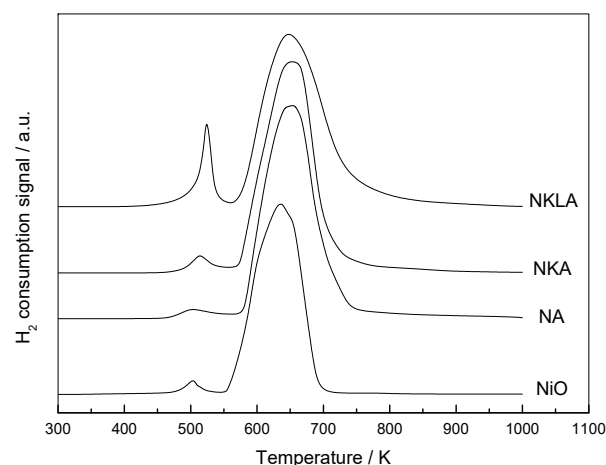


Figure 2. TPR profiles of the three catalysts for NA, NKA and NKLA.

Otherwise, here we also found that the addition of La improved the terminal reduction temperature of the catalyst. This can perhaps be attributed to the presence of adsorbed H₂O molecules or hydroxyl groups on the surface. Richardson and Twigg, in discussing the reduction behaviors of the impregnated La-promoted NiO/ α -Al₂O₃ catalysts, also observed the retardation effect of the La₂O₃ additive [29].

2.1.3. XRD

Figure 3 shows the XRD patterns of the NA, NKA and NKLA samples before and after reduction. There were only α -alumina and nickel oxide detected in all of the unreduced catalysts (as shown in Figure 3a); that is, the addition of K₂O and La₂O₃ did not affect the phases of NA. La containing phases, such as La₂O₃ (05-0602, JCPDS), LaAlO₃ (85-1071, JCPDS) and LaAl₁₂O₁₉ (77-0335, JCPDS), were not detected, although its presence was reported by other authors [30]. This indicates that the La species dispersed very well and/or did not react with the support due to low temperature calcination. It is noteworthy that the intensity of NiO diffraction peaks decreased markedly due to La₂O₃, whereas it was not affected by K₂O.

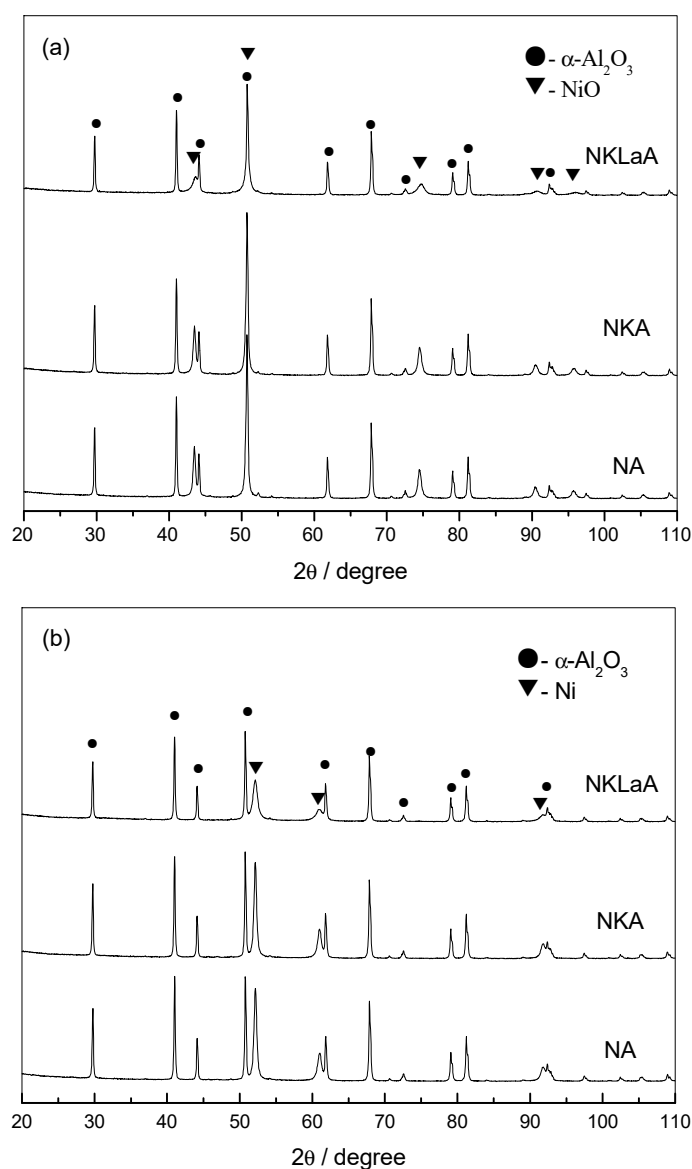


Figure 3. XRD patterns of NA, NKA and NKLA: (a) before reduction; (b) after reduction.

Figure 3b presents the XRD diffraction patterns of NA, NKA and NKLA after reduction. Apart from α - Al_2O_3 , only metal nickel was detected. Similar to the unreduced catalysts, the addition of La_2O_3 led to the decrease of metal nickel. According to the calculation of the main X-ray diffraction peak of NiO (200) by the Scherrer Equation, the Ni particle sizes were 28.0 nm, 28.3 nm and 16.0 nm in NA, NKA and NKLA catalysts, respectively.

2.1.4. FE-TEM

Figure 4 shows the TEM pictures of the catalysts reduced to 623 K for 2 h. It is obvious that the Ni particles were dispersed on α - Al_2O_3 particles in every catalyst. However, there was a remarkable difference in the nickel particles' size and the distribution for NA, NKA and NKLA. Compared with NA and NKA, NKLA had a narrower nickel particle size distribution and much smaller nickel particles. Though nickel crystallite sizes observed from images are different from those calculated with the Scherrer formula to a certain extent, the effect of the promoters was similar; that is, La_2O_3 markedly improved the nickel dispersion, and K_2O did not affect the nickel particles size.

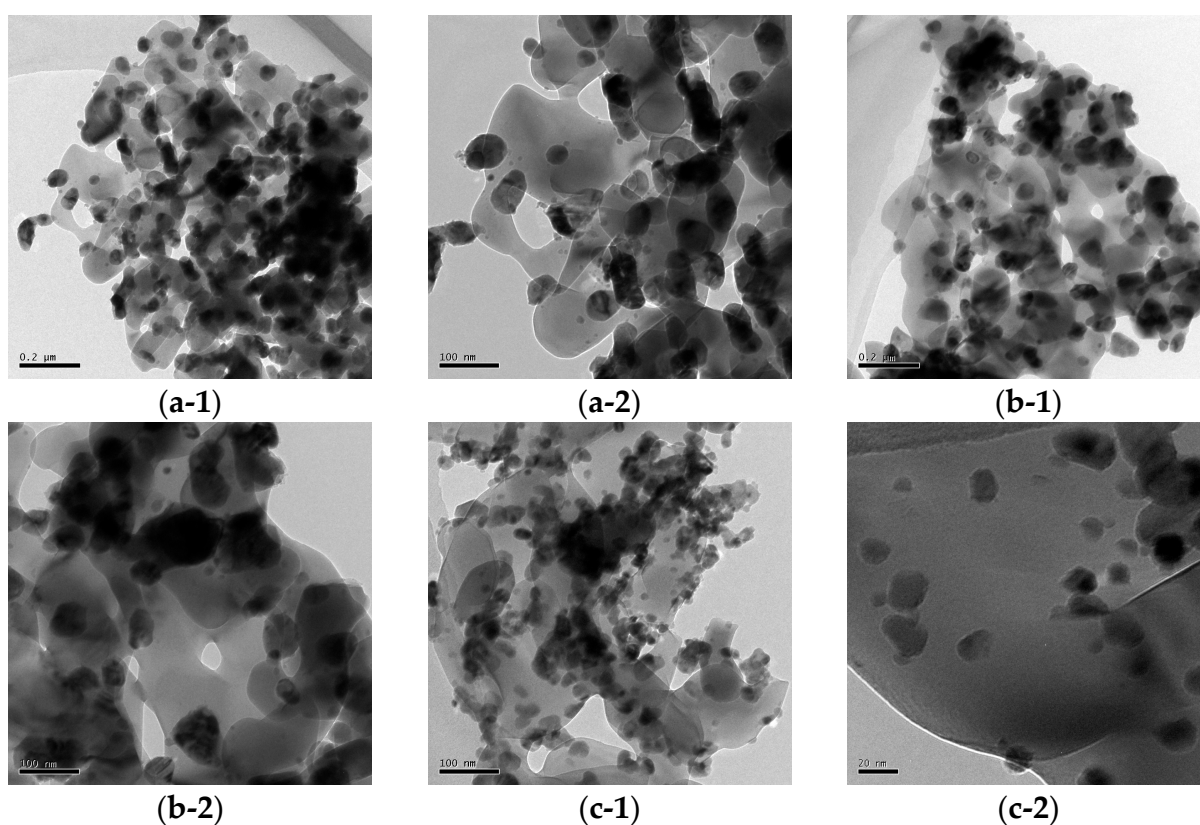


Figure 4. TEM pictures of (a-1,a-2) NA; (b-1,b-2) NKA; (c-1,c-2) NKLA reduced to 623 K for 2 h.

2.1.5. H_2 -Chemisorption and H_2 -TPD

Table 1 also lists the H_2 -chemisorption amounts of the reduced NA, NKA and NKLA catalysts. The H_2 chemisorption amounts of NA, NKA and NKLA were 9.4, 12.9 and 53.4 $\mu\text{mol H}_2/\text{g.cat}$, respectively. NKA had slightly higher H_2 chemisorption amount than NA, while the H_2 chemisorption amount of NKLA was about 5.7 times that of NA; that is, La_2O_3 greatly increased the H_2 chemisorption amount of NA. The results were consistent with the nickel particle sizes on NA, NKA and NKLA catalysts as shown in XRD and TEM. Usually, the smaller the nickel particles, the larger the nickel surface area and the more H_2 is chemisorbed.

After the H_2 -chemisorption measurement, the H_2 -TPD experiments were performed, and the H_2 -TPD profiles of the NA, NKA and NKLA catalysts are shown in Figure 5. For

all samples, H₂ desorption occurred below 573 K, which is generally attributed to hydrogen species adsorbed on the metal nickel particles [31–35]. No H₂-desorption peaks appeared at higher temperature indicating that there was no spilt-over hydrogen species and/or the subsurface hydrogen species [36].

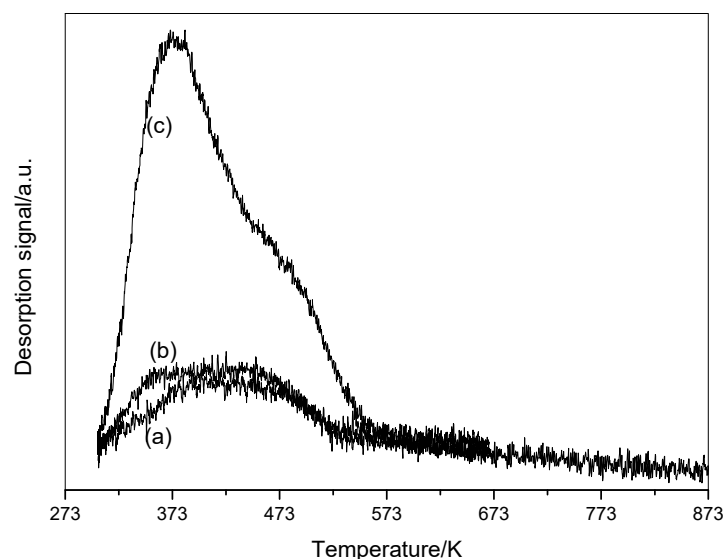


Figure 5. H₂-TPD profiles of (a) NA; (b) NKA; (c) NKLA catalyst.

In short, XRD and TEM results have shown that an apparent decrease in the Ni⁰ particle size as the La₂O₃ promoter was introduced, while the catalyst doped with only K nearly did not change, implying that the La₂O₃ strained the sintering of nickel during the reduction process. This also tested the fact that lanthanide is usually used as a structural promoter to increase the dispersion of metal (e.g., Ni), causing enhanced sintering resistance, leading to smaller nickel crystallites in Ni/Al₂O₃ catalysts [27]. Moreover, according to the H₂-chemisorption experiments, perhaps the bigger H₂ uptakes for the catalyst NKLA than NA and NKA catalysts should not be interpreted in terms of a partial improvement of the hydrogen adsorption capacity, but instead, in terms of change of the particle size. Although the metal dispersion and the surface structure of the metal particles may affect the catalyst performance [37], according to usual conditions, the smaller the nickel particles, the larger the nickel surface area and the more chemisorbed H₂, which was consistent with the catalytic performance and the average size of nickel particles in the catalysts. All the data from different approaches for the determination of the average metal particles' size made the agreement between the values obtained from H₂-chemisorption and those provided by independent techniques (TEM or XRD).

2.2. Catalyst Performance

2.2.1. Effects of Promoters

Figure 6 shows the hydrogenation performance of NA, NKA and NKLA catalysts. All of the catalysts had a high initial ADN conversion; however, they deactivated along with the reaction to different extents. The NA catalyst showed the most drastic decrease of ADN conversion from 99.9 to 52.3% during the first 6 h. Over NKA and NKLA, ADN conversion was similar and did not remarkably change during the first 7.0 h, and then it decreased gradually. However, a higher conversion loss was observed for NKA. For example, ADN conversion (86.1%) over NKA was 7% lower than that (93.1%) over NKLA at the tenth hour. ADN conversion decreased to about 40.2% at the thirtieth hour over NKA, while that over NKLA was 63.6% at the fortieth hour and fell to about 40.1% at the fiftieth hour.

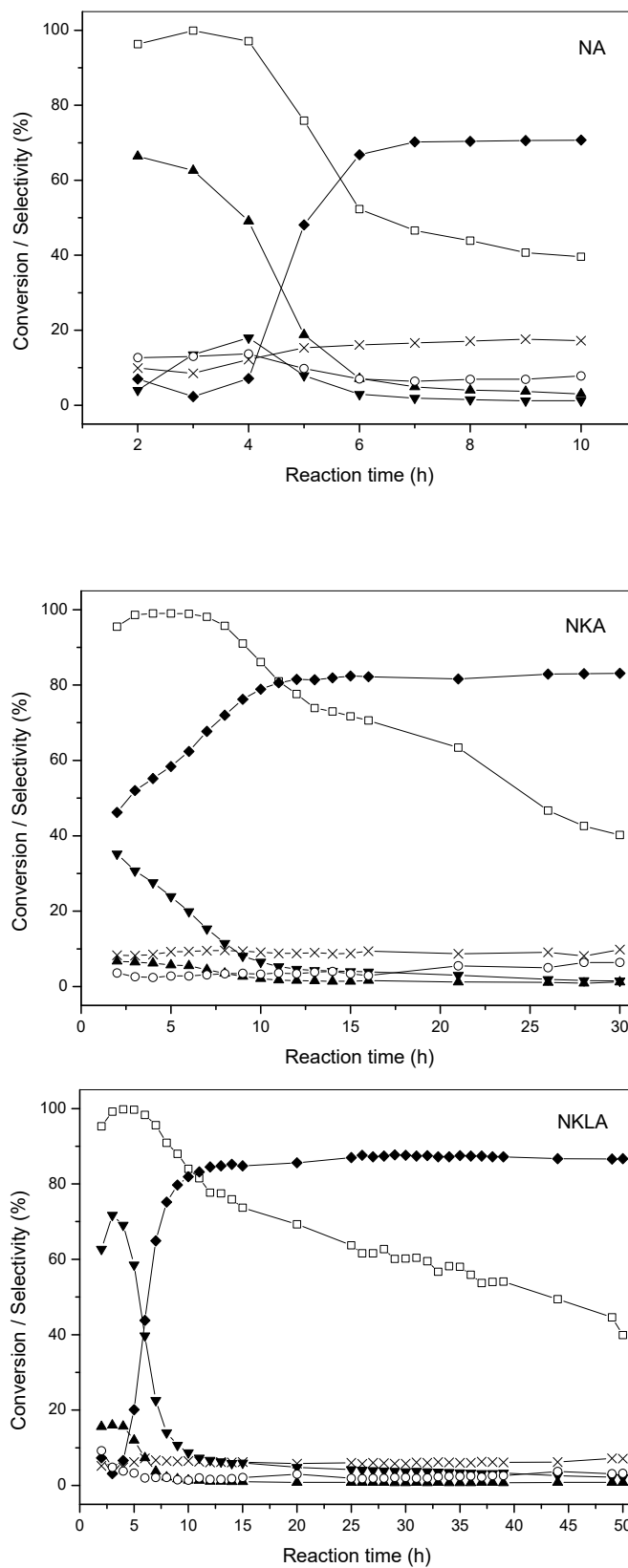


Figure 6. Reactivity of NA, NKA and NKLA catalysts in the hydrogenation of ADN. Symbols: ADN conversion (□), cracking products selectivity (×), ACH selectivity (▲), HMDA selectivity (▼), ACN selectivity (◆) and condensation products selectivity (○).

As shown in Figure 6, apart from the aim product ACN, the main by-products were hexamethylenediamine (HMDA) and azacycloheptane (ACH) during the partial hydrogenation of ADN. ACN selectivity increased with the reaction time over every catalyst until it reached a constant, which was much lower over the NA catalyst than that over the NKA and NKLA catalysts. Eventually, ACN selectivity was about 70% over the NA catalyst and it exceeded 80% over the NKA and NKLA catalysts, with a slightly higher ACN selectivity over NKLA than that of NKA. It was worth noticing that selectivity with respect to HMDA and ACH followed the opposite trend for ACN selectivity, respectively, indicating different structural requirements for the active sites responsible for the production of ACN with respect to those of HMDA and ACH. Besides, the initial ACH selectivity was much higher than the initial HMDA selectivity over NA, while the contrary case occurred over NKA and NKLA.

The hydrogenation of nitriles is a complex process, which consists of a complex set of reactions, such as the hydrogenations of nitriles to imines and amines, the condensations between imines and amines, and deaminations and cyclization, involving a number of reactive intermediates. Additionally, the presence of a second nitrile group can lead to intermolecular or intramolecular condensation reactions as well, thus giving rise to a wide product spectrum. Due to the ring structure of the imine–amine intramolecular condensation product, deamination and dehydrogenation reactions assume an important role in the determination of the final product. During the process of hydrogenation of ADN as shown in Figure 7 [38], ADN can be initially hydrogenated to ACN and then finally to HMDA. Over basic surface sites, ADN can form 2-methylamino-1-aminocyclopentane via Thorpe–Ziegler cyclization. Other unwanted reactions include the formation of 1,2-diaminocyclohexane (DCH) by a diamine intermediate as well as cyclic and linear Schiff bases [39]. DCH can be avoided by blocking the most active sites with NaOH [40] or deposited coke from the reaction [41], and the Schiff base formation is inhibited by the presence of ammonia or group IA hydroxides [42,43]. Of course, the addition of alkali metal may play a negative effect on the hydrogenation reaction to a certain extent. Moreover, several reasons can be given for the negative effect of basic additives. The presence of alkali could depress the (acid catalyzed) elimination of ammonia from intermediate and, therefore, lead to the accumulation of reactive intermediates and to uncontrolled condensation reactions. Alternatively, the residence time of basic compounds on the catalytic surface could be negatively affected by the basicity of the catalyst. The lower residence time on the metal surface decreases the chance of the hydrogenation, dehydrogenation and deamination of reactive intermediates, which, on leaving the catalytic surface, may undergo condensations in the vapor phase. A third reason might be that base-catalyzed reactions (e.g., Thorpe and Thorpe–Ziegler reactions), which probably take place on the support, are favored by the presence of strong basic centers. This enhanced formation of C–C by-products, which contain amino groups and are partly unsaturated, decreases the selectivity to desired products and simultaneously increases the amount of potentially strongly adsorbing compounds.

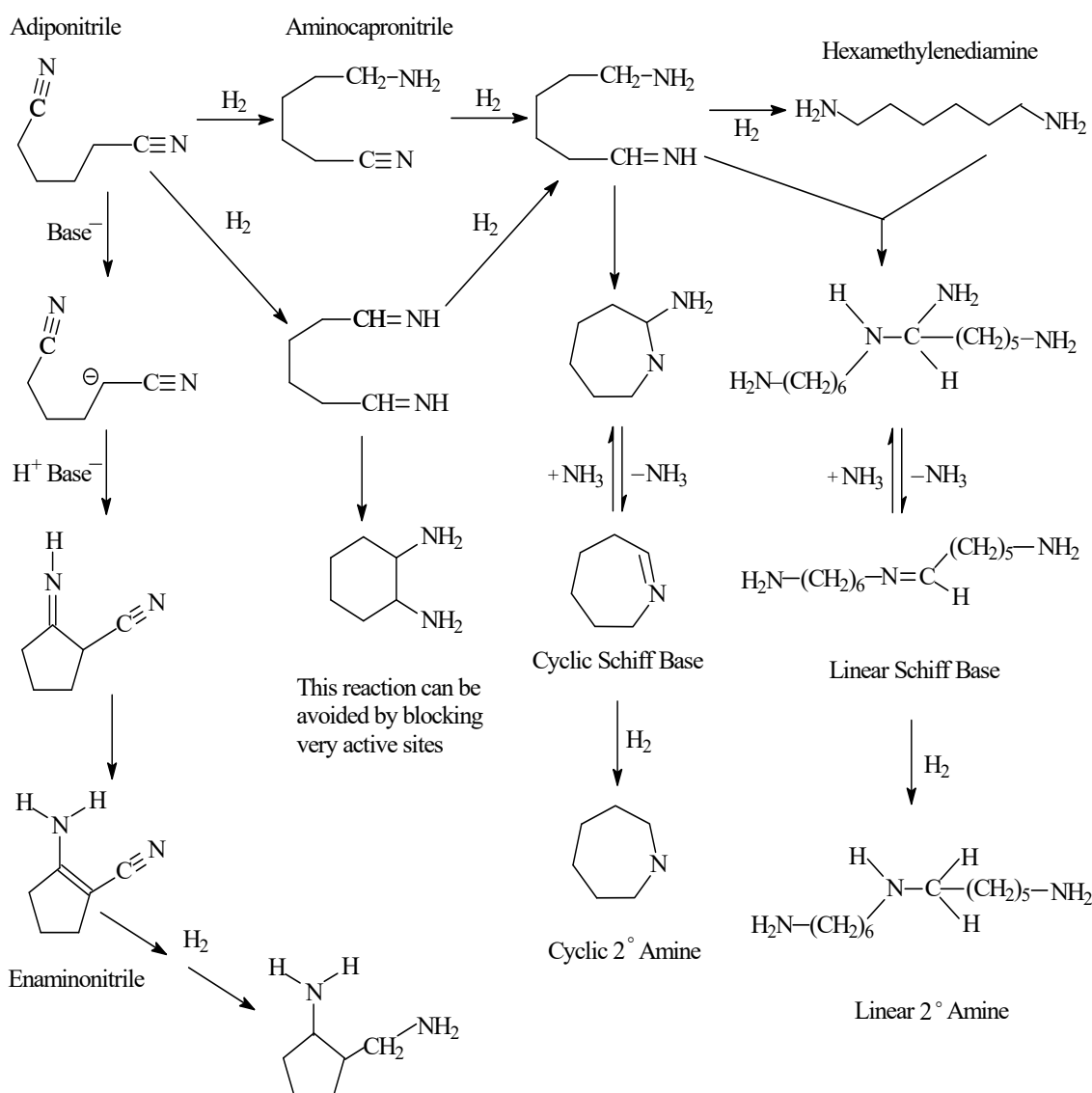


Figure 7. The possible hydrogenation of ADN.

Figure 6 indicates that K_2O improved not only catalyst stability but also ACN selectivity, while La_2O_3 mainly improved catalyst stability. Several reasons can be given for the positive effect of K_2O . K_2O could increase the basic property of the catalyst surface [21], which favored the desorption of the hydrogenation products that were of basic substance and tended to avoid the deactivation of the catalyst. Thus, the longer residence time of the imines would favor hydrogenation reactions, producing lighter by-products as well as some higher molecular side reactions such as imines trimerization, yielding heavy compounds which stay on the metallic surface and block catalytically active sites. In addition, taking into account the electronic effect, K donated an electron to Ni and made the Ni atom electron-enriched [13]. The Ni-rich electrons were in favor of the dissolved adsorption of H_2 . Moreover, there is the competitive adsorption between H_2 and ADN on the Ni active phase, while the Ni-rich electrons could weaken the adsorption of ADN due to the repulsion of the $C\equiv N$ band with lone pair electrons, which was also a benefit of the adsorption of H_2 . According to the Braun mechanism [44], the Ni-rich electrons could also inhibit the condensation reactions and thus serve to prevent or delay the rapid deactivation of the catalyst. In short, the addition of K_2O favored the hydrogenation of ADN and desorption of ACN, inhibiting the further conversion of ACN and avoiding other side reactions. Thus, the ACN selectivity and the catalyst stability were increased.

As shown in the TEM images (Figure 4), there was not a remarkable difference in the size of nickel particles between NA and NKA, while the nickel particles over NKLA were smaller than that over NA and NKA, indicating that La_2O_3 improved the nickel dispersion. As a result, the amount of H_2 -chemisorption was larger for NKLA, and it was 9.4, 12.9 and 53.4 $\mu\text{mol/g.cat}$ for NA, NKA and NKLA, respectively. Moreover, the La_2O_3 was a weak basic substance, which was also a benefit of improving the reactivity of the catalyst. Due to the above reasons, when $\text{Ni}/\alpha\text{-Al}_2\text{O}_3$ was co-promoted with La_2O_3 and K_2O , its performance for the partial hydrogenation of ADN increased remarkably. In short, with our catalyst with a high metal dispersion, it was possible to achieve good ADN conversion and high ACN selectivity.

2.2.2. Catalyst Deactivation and Regeneration

The hydrogenation of ADN is a complex reaction system, and the catalyst used in this system tends to be deactivated. While so far, the deactivation phenomenon and reactivation information are not easily available in the open literature, here, we made a primary investigation of the deactivation of the NKLA catalyst in the hydrogenation of ADN and studied the regeneration method of the deactivated catalyst.

Figure 8 depicts the TG curve of the used NKLA catalyst. In the TG profile, there were mainly three weight-change stages: a 5.8 wt.% mass-loss stage (from room temperature to 650 K) was owed to the desorption of the free solvent and the oxidation of some organic compounds; a 0.2 wt.% mass-increase stage (from 650 K to 705 K) was attributed to the oxidation of metallic nickel; and the third stage (about 1.2 wt.% mass loss, above 705 K) was due to the oxidation of the organic species on the catalyst. Because the oxidation of the metallic nickel and some of the organic species occurred in the similar temperature range, the mass-increase stage due to the oxidation of metallic nickel in the used one could be masked by the mass-loss stage of the oxidation of the organic species.

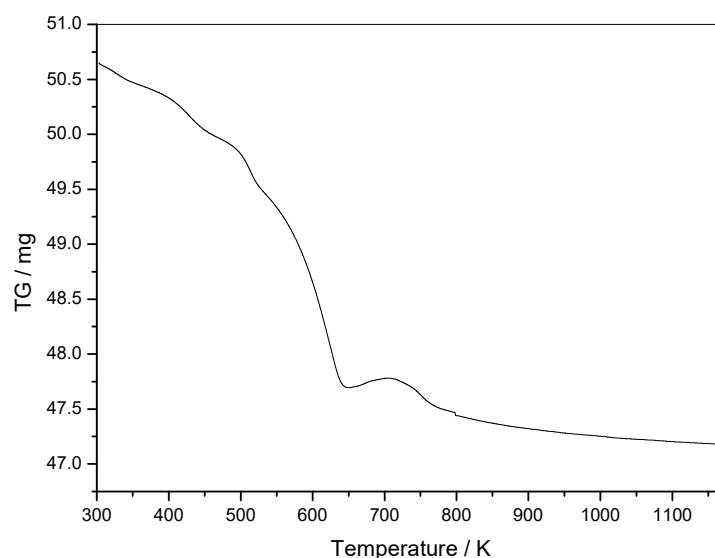


Figure 8. TG curves of the deactivated NKLA catalyst.

Aside, Table 2 lists the ESEM-EDX analysis results of the fresh catalyst and the used one, which showed that there was an increase in C and N on the deactivated sample compared to the fresh one.

Table 2. The EDX data of the fresh NKLA catalyst and the deactivated one.

The Fresh Catalyst			The Deactivated Catalyst		
Element	Weight/%	Atom Ratio/%	Element	Weight Ratio/%	Atom Content/%
C K	/	/	C K	11.15	19.44
N K	/	/	N K	1.00	1.50
O K	39.49	58.82	O K	37.28	48.82
Al K	35.88	31.68	Al K	30.01	23.30
K K	0.02	0.01	K K	0.18	0.10
Ni K	22.47	9.12	Ni K	18.32	6.54
La L	2.13	0.37	La L	2.06	0.31
Total	100.00		Total	100.00	

EDX results were consistent with the conclusions drawn from the literature. For example, Alan M. Allgeier et al. [45] pointed out that Raney Ni deactivated during ADN hydrogenation reactions in the absence of the base as a result of the deposition of polyamines, which physically blocked the surface. BASF corporation [5] also claimed that low polyamines were the main reason for the deactivation of the Ni-based catalyst in the hydrogenation of ADN, but it did not provide vigorous evidence for this. Otherwise, some authors also found in the hydrogenation of acetonitrile that the formation of surface nickel carbides was the major cause of the loss of activity with time on stream. The presence of partly dehydrogenated species was a second factor causing the loss of activity. The resulting species were strongly adsorbed on the nickel surface and blocked some of the active sites for hydrogenation [46].

For an industrial catalyst, one of the key factors is the regeneration of the deactivated catalyst. S. Alini et al. [19] found that the slight decrease in and conversion can be recovered by treating the catalysts after their use with ethanol and H₂ in the gaseous phase, but the ACN selectivity is only partially recovered. Lei Ye et al. [47] also pointed out in the hydrogenation of acetonitrile that the treatment of the deactivated catalyst with hydrogen at an elevated temperature (>200 °C) restored both the catalytic activity and the selectivity of the catalyst.

Additionally, the performance of the renewed NKLA catalyst after some reuses of the same batch of NKLA is reported in Figure 9. The slight decrease in ADN conversion can be recovered by treating the catalyst after their use with gaseous H₂ in situ, though after use, the catalyst deactivated more rapidly. Yet, after reduction with gaseous H₂, the initial ACN selectivity is partially improved and the final of that reaches about the same value. Figure 9 showed only the hydrogenation results of the fifth run after reduction with H₂ in situ. Aside from this, when the deactivated catalyst was washed only with absolute ethanol, the initial activity decreased and finally achieved the same or a higher value with the time, while the ACN selectivity decreased in the end. Thirdly, the ADN conversion and the ACN selectivity both decreased when the deactivated catalyst was calcined and reduced in the H₂ atmosphere again. The deactivation cause and regeneration research will be in further studies, and the next paper will describe the phenomenon in detail.

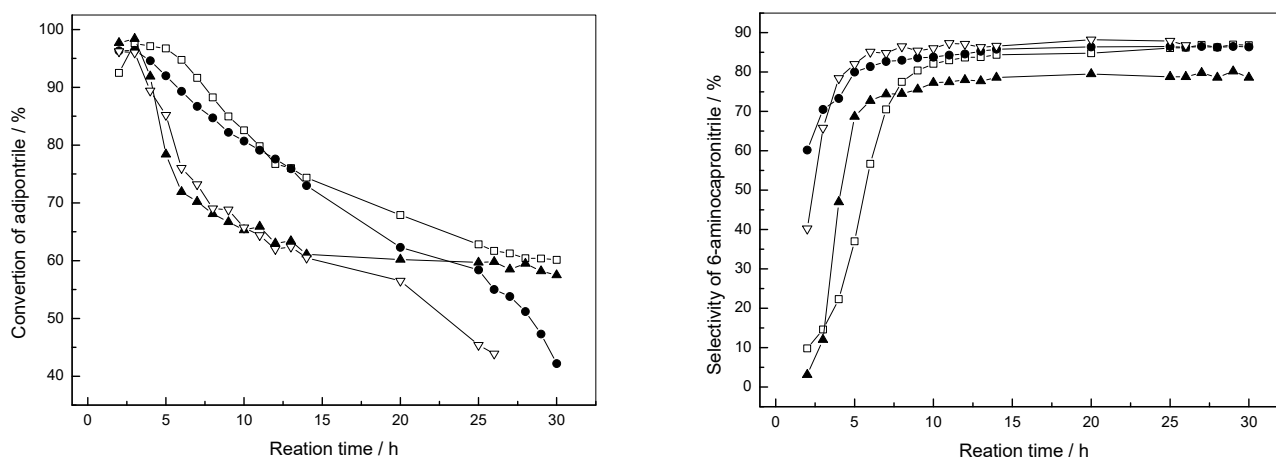


Figure 9. Catalytic performance of NKLA catalyst for the fresh catalyst (\square) and the fifth run on the same batch (\bullet) and the deactivated ones washed only with absolute ethanol (\blacktriangle) and calcined and reduced in H_2 again (∇).

3. Experimental Work

3.1. Catalyst Preparation

The $\alpha\text{-Al}_2\text{O}_3$ -supported catalysts were prepared by the impregnation method. The porous $\alpha\text{-Al}_2\text{O}_3$ was incipiently impregnated with an aqueous solution of $\text{Ni}(\text{NO}_3)_2$ or an aqueous solution of $\text{Ni}(\text{NO}_3)_2$ and the additive nitrate, and left at room temperature for 24 h. The sample was then dried at 393 K for 12 h and calcined in air at 623 K for 4 h. Since the target Ni loading was about 25 wt.% and a single impregnation gave about 15–18 wt.% loading, two separate impregnation steps were necessary. $\text{NiO}/\alpha\text{-Al}_2\text{O}_3$ catalysts un-promoted or promoted with K_2O or K_2O and La_2O_3 were labeled as NA, NKA and NKLA, respectively. Based on $\alpha\text{-Al}_2\text{O}_3$, the mass contents of Ni, K and La were set at 25, 0.1 and 3%, respectively.

3.2. Catalyst Characterization

N_2 adsorption and desorption isotherms of the samples were measured on a Micromeritics ASAP 2020 automated physisorption instrument (Micromeritics, Norcross, GA, USA) at 77 K. Prior to the measurement, the samples were degassed in a vacuum at 573 K for 2 h. The specific surface area was determined by the Brunauer–Emmett–Teller (BET) method. The pore volume and pore size were determined from the desorption branch of the N_2 adsorption isotherm.

X-ray powder diffraction (XRD) patterns of the samples were measured on a PANalytical's X'Pert PRO powder X-ray diffractometer (Malvern PANalytical Ltd., Almelo, The Netherlands) with $\text{CoK}\alpha$ radiation. The average nickel crystallite size was estimated from XRD line-broadening by employing the Scherrer equation, $d = (0.9 \lambda) / (\beta \cos\theta)$, where d is the crystallite size, λ is the wavelength of the radiation, β is the full width at half maximum of the peak and θ is the Bragg angle.

Temperature programmed reduction (TPR) was carried out in a tubular quartz reactor, where 100 mg catalyst was loaded in the thermostatic zone. The reduction was conducted in a flow of a $\text{H}_2\text{-N}_2$ mixture (volume ratio, 10:90) at a heating rate of 15 K/min. The consumption of hydrogen was detected using a thermal conductivity detector (TCD).

The nickel crystallites over the reduced catalysts were observed on a Field Emission Gun Transmission Electron Microscope (FETEM, PHILIPS Tecnai G² F20, FEI, Oregon, USA).

Hydrogen chemisorption was performed on a Thermo Finnegan TPD/R/O 1100 instrument (Waltham, MA, USA). After reduction at 623 K for 2 h, the hydrogen on the nickel surface was removed with 20 mL/min of He (99.999%) for 30 min. The sample was cooled to 298 K under a He stream, and the He stream was then switched to N_2

(99.999%). After the TCD was stable under the N₂ flow, H₂ pulses (100 µL/pulse) were injected until the effluent area of consecutive pulses was constant. The dispersion of Ni was calculated assuming a stoichiometry of one hydrogen molecule adsorbed on per two surface nickel atoms [46], and it was given by $D = Ni_s/Ni_t = H/Ni$. The metal surface area (S_m , m².g⁻¹), dispersion (D, %) and metal particle size (d, nm) were determined from the H₂ chemisorption amount. H₂-temperature programmed desorption (H₂-TPD) was performed on the basis of H₂-chemisorption, and it was performed in a N₂ flow of 50 mL/min and conducted between 303 and 1023 K with a heating rate of 10 K/min. The evolved H₂ was detected by an on-line thermal conductivity detector.

3.3. Activity Test

The activity test was carried out in a tubular stainless steel fixed-bed reactor (12 mm ID) in a continuous process under atmospheric pressure, 453 K, and in the absence of ammonia conditions. Before reaction, the catalyst (4.0 g) was reduced by hydrogen (6 l/h) at 623 K for 4 h, and when the temperature decreased to the designated value, the ADN solution in EtOH (volume ratio of ADN to EtOH as 0.25, 5 mL/h) and hydrogen (6.5 l/h) was fed into the reactor. The qualitative analysis of the product samples was carried out on a GC6890-MS5973 (Agilent, Santa Clara, CA, USA) and the quantitative analysis on a gas chromatograph equipped with a flame ionization detector (FID) and a SE-54 capillary column (30 m).

4. Conclusions

Two promoters of K₂O and La₂O₃ were doped into the Ni/α-Al₂O₃ catalyst prepared with the impregnation method. By reducing the precursor in an H₂ atmosphere, it is possible to obtain a catalyst with a very high metal dispersion and small Ni crystallites. In the hydrogenation of adiponitrile, the Ni-based catalyst doped with K₂O or K₂O and La₂O₃ showed a better performance to produce ACN than the Ni/α-Al₂O₃ catalyst, i.e., K₂O not only improved the stability of the catalysts but also improved ACN selectivity, while La₂O₃ mainly improved the catalysts' stability. On the one hand, K₂O could increase the basic property of the catalyst surface; on the other hand, K donated an electron to Ni and made the Ni atom electron-enriched, all of which favored the desorption of ACN and inhibited the further conversion of ACN. XRD, TEM and H₂-chemisorption results indicated that La₂O₃ improved the nickel dispersity and the amount of hydrogen chemisorption. Due to the above reasons, when Ni/α-Al₂O₃ was co-promoted with La₂O₃ and K₂O, its performance for the partial hydrogenation of ADN increased remarkably.

The activity of the deactivated Ni-based catalyst in the hydrogenation of adiponitrile could be recovered by reducing in the H₂ gas phase and by washing with absolute ethanol, although the regenerated catalyst may be deactivated more rapidly. The deposition of the compound including C and N is perhaps the main reason for the deactivation, and further and in-depth investigations are ongoing.

Author Contributions: Writing—review and editing, L.Z. and C.W.; visualization, J.Z.; supervision, J.C.; project administration, Z.N.; funding acquisition, X.L. All authors have read and agreed to the published version of the manuscript.

Funding: This research was funded by the National Natural Science Foundation Project of China (grant number 52066017) and the Key R&D and Transformation Plan of Qinghai Province (grant number 2022-GX-C13).

Data Availability Statement: The data presented in this study is included in the article.

Conflicts of Interest: The authors declare no conflict of interest.

References

1. Nwosu, U.; Wang, A.; Palma, B.; Zhao, H.; Khan, M.A.; Kibria, M.; Hu, J. Selective biomass photo reforming for valuable chemicals and fuels: A critical review. *Renew. Sustain. Energy Rev.* **2021**, *148*, 111266. [[CrossRef](#)]

2. Davis, K.A.; Yoo, S.; Shuler, E.W.; Sherman, B.D.; Lee, S.; Leem, G. Photocatalytic hydrogen evolution from biomass conversion. *Nano Converg.* **2021**, *8*, 256. [[CrossRef](#)] [[PubMed](#)]
3. Ibrahim, N.; Kamarudin, S.K.; Minggu, L.J. Biofuel from biomass via photo-electrochemical reactions: An overview. *J. Power Sources* **2014**, *259*, 33–42. [[CrossRef](#)]
4. Ruppert, A.M.; Weinberg, K.; Palkovits, R. Hydrogenolysis Goes Bio: From Carbohydrates and Sugar Alcohols to Platform Chemicals. *Angew. Chem. Int. Ed.* **2012**, *51*, 2564–2601. [[CrossRef](#)]
5. Yu, Z.; Lu, X.; Wang, X.; Xiong, J.; Li, X.; Zhang, R.; Ji, N. Metal-Catalyzed Hydrogenation of Biomass-Derived Furfural: Particle Size Effects and Regulation Strategies. *ChemSuschem* **2020**, *13*, 5185–5198. [[CrossRef](#)]
6. Hu, L.; He, A.; Liu, X.; Xia, J.; Xu, J.; Zhou, S.; Xu, J. Biocatalytic Transformation of 5-Hydroxymethylfurfural into High-Value Derivatives: Recent Advances and Future Aspects. *ACS Sustain. Chem. Eng.* **2018**, *6*, 15915–15935. [[CrossRef](#)]
7. Wang, H.; Zhu, C.; Li, D.; Liu, Q.; Tan, J.; Wang, C.; Cai, C.; Ma, L. Recent advances in catalytic conversion of biomass to 5-hydroxymethylfurfural and 2,5-dimethylfuran. *Renew. Sustain. Energy Rev.* **2019**, *103*, 227–247. [[CrossRef](#)]
8. Hu, L.; Xu, J.; Zhou, S.; He, A.; Tang, X.; Lin, L.; Xu, J.; Zhao, Y. Catalytic Advances in the Production and Application of Biomass-Derived 2,5-Dihydroxymethylfuran. *ACS Catal.* **2018**, *8*, 2959–2980. [[CrossRef](#)]
9. Li, C.; Na, Y. Recent Advances in Photocatalytic Oxidation of 5-Hydroxymethylfurfural. *ChemPhotoChem* **2021**, *5*, 502–511. [[CrossRef](#)]
10. Wu, X.; Xie, S.; Zhang, H.; Zhang, Q.; Sels, B.F.; Wang, Y. Metal Sulfide Photocatalysts for Lignocellulose Valorization. *Adv. Mater.* **2021**, *33*, 2007129. [[CrossRef](#)]
11. Wu, X.; Luo, N.; Xie, S.; Zhang, H.; Zhang, Q.; Wang, F.; Wang, Y. Photocatalytic transformations of lignocellulosic biomass into chemicals. *Chem. Soc. Rev.* **2020**, *49*, 6198–6223. [[CrossRef](#)] [[PubMed](#)]
12. Marzo, L.; Pagire, S.K.; Reiser, O.; König, B. Photokatalyse mit sichtbarem Licht: Welche Bedeutung hat sie für die organische Synthese? *Angew. Chem. Int. Ed.* **2018**, *130*, 10188–10228. [[CrossRef](#)]
13. Nie, J.; Xie, J.; Liu, H. Efficient aerobic oxidation of 5-hydroxymethylfurfural to 2,5-diformylfuran on supported Ru catalysts. *J. Catal.* **2013**, *301*, 83–91. [[CrossRef](#)]
14. Han, G.; Jin, Y.; Burgess, R.A.; Dickenson, N.E.; Cao, X.; Sun, Y. Visible-Light-Driven Valorization of Biomass Intermediates Integrated with H₂ Production Catalyzed by Ultrathin Ni/CdS Nanosheets. *J. Am. Chem. Soc.* **2017**, *139*, 15584–15587. [[CrossRef](#)]
15. Zhang, M.; Yu, Z.; Xiong, J.; Zhang, R.; Liu, X.; Lu, X. One-step hydrothermal synthesis of Cd_xIn_yS_(x+1.5y) for photocatalytic oxidation of biomass-derived 5-hydroxymethylfurfural to 2,5-diformylfuran under ambient conditions. *Appl. Catal. B* **2022**, *300*, 120738. [[CrossRef](#)]
16. Bao, X.; Liu, M.; Wang, Z.; Dai, D.; Wang, P.; Cheng, H.; Liu, Y.; Zheng, Z.; Dai, Y.; Huang, B. Photocatalytic Selective Oxidation of HMF Coupled with H₂ Evolution on Flexible Ultrathin g-C₃N₄ Nanosheets with Enhanced N-H Interaction. *ACS Catal.* **2022**, *12*, 1919–1929. [[CrossRef](#)]
17. Tan, Y.; Chai, Z.; Wang, B.; Tian, S.; Deng, X.; Bai, Z.; Chen, L.; Shen, S.; Guo, J.; Cai, M.; et al. Boosted Photocatalytic Oxidation of Toluene into Benzaldehyde on CdIn₂S₄-CdS: Synergetic Effect of Compact Heterojunction and S-Vacancy. *ACS Catal.* **2021**, *11*, 2492–2503. [[CrossRef](#)]
18. Liu, M.; Chen, Y.; Su, J.; Shi, J.; Wang, X.; Guo, L. Photocatalytic hydrogen production using twinned nanocrystals and an unanchored NiS_x co-catalyst. *Nat. Energy* **2016**, *1*, 16151. [[CrossRef](#)]
19. Kar, P.; Farsinezhad, S.; Mahdi, N.; Zhang, Y.; Obuekwe, U.; Sharma, H.; Shen, J.; Semagina, N.; Shankar, K. Enhanced CH₄ yield by photocatalytic CO₂ reduction using TiO₂ nanotube arrays grafted with Au, Ru, and ZnPd nanoparticles. *Nano Res.* **2016**, *9*, 3478–3493. [[CrossRef](#)]
20. Lang, Q.; Yang, Y.; Zhu, Y.; Hu, W.; Jiang, W.; Zhong, S.; Gong, P.; Teng, B.; Zhao, L.; Bai, S. High-index facet engineering of PtCu cocatalysts for superior photocatalytic reduction of CO₂ to CH₄. *J. Mater. Chem.* **2017**, *A5*, 6686–6694. [[CrossRef](#)]
21. Zeng, Z.; Yan, Y.; Chen, J.; Zan, P.; Tian, Q.; Chen, P. Boosting the Photocatalytic Ability of Cu₂O Nanowires for CO₂ Conversion by MXene Quantum Dots. *Adv. Funct. Mater.* **2019**, *29*, 1806500. [[CrossRef](#)]
22. Xiao, R.; Zhao, C.; Zou, Z.; Chen, Z.; Tian, L.; Xu, H.; Tang, H.; Liu, Q.; Lin, Z.; Yang, X. In situ fabrication of 1D CdS nanorod/2D Ti₃C₂ MXene nanosheet Schottky heterojunction toward enhanced photocatalytic hydrogen evolution. *Appl. Catal. B* **2020**, *268*, 118382. [[CrossRef](#)]
23. Li, J.; Li, Y.; Zhang, F.; Tang, Z.; Xu, Y. Visible-light-driven integrated organic synthesis and hydrogen evolution over 1D/2D CdS-Ti₃C₂T_x MXene composites. *Appl. Catal. B* **2020**, *269*, 118783. [[CrossRef](#)]
24. Yang, C.; Tan, Q.; Li, Q.; Zhou, J.; Fan, J.; Li, B.; Sun, J.; Lv, K. 2D/2D Ti₃C₂ MXene/g-C₃N₄ nanosheets heterojunction for high efficient CO₂ reduction photocatalyst: Dual effects of urea. *Appl. Catal. B* **2020**, *268*, 118738. [[CrossRef](#)]
25. Xu, Y.; Yang, M.; Chen, B.; Wang, X.; Chen, H.; Kuang, D.; Su, C. A CsPbBr₃ Perovskite Quantum Dot/Graphene Oxide Composite for Photocatalytic CO₂ Reduction. *J. Am. Chem. Soc.* **2017**, *139*, 5660–5663. [[CrossRef](#)] [[PubMed](#)]
26. Zuo, G.; Wang, Y.; Teo, W.L.; Xie, A.; Guo, Y.; Dai, Y.; Zhou, W.; Jana, D.; Xian, Q.; Dong, W.; et al. Ultrathin ZnIn₂S₄ Nanosheets Anchored on Ti₃C₂T_x MXene for Photocatalytic H₂ Evolution. *Angew. Chem. Int. Ed.* **2020**, *59*, 11287–11292. [[CrossRef](#)] [[PubMed](#)]
27. Cao, S.; Shen, B.; Tong, T.; Fu, J.; Yu, J. 2D/2D Heterojunction of Ultrathin MXene/Bi₂WO₆ Nanosheets for Improved Photocatalytic CO₂ Reduction. *Adv. Funct. Mater.* **2018**, *28*, 1800136. [[CrossRef](#)]
28. Chen, P.; Liu, F.; Ding, H.; Chen, S.; Chen, L.; Li, Y.; Au, C.; Yin, S. Porous double-shell CdS@C₃N₄ octahedron derived by in situ supramolecular self-assembly for enhanced photocatalytic activity. *Appl. Catal. B* **2019**, *252*, 33–40. [[CrossRef](#)]

29. Liu, F.; Xiao, C.; Meng, L.; Chen, L.; Zhang, Q.; Liu, J.; Shen, S.; Guo, J.; Au, C.; Yin, S. Facile Fabrication of Octahedral CdS-ZnS by Cation Exchange for Photocatalytic Toluene Selective Oxidation. *ACS Sustain. Chem. Eng.* **2020**, *8*, 1302–1310. [[CrossRef](#)]
30. Wang, S.; Guan, B.Y.; Lu, Y.; Lou, X.W.D. Formation of Hierarchical In₂S₃-CdIn₂S₄ Heterostructured Nanotubes for Efficient and Stable Visible Light CO₂ Reduction. *J. Am. Chem. Soc.* **2017**, *139*, 17305–17308. [[CrossRef](#)]
31. Pan, A.; Ma, X.; Huang, S.; Wu, Y.; Jia, M.; Shi, Y.; Liu, Y.; Wangyang, P.; He, L.; Liu, Y. CsPbBr₃ Perovskite Nanocrystal Grown on MXene Nanosheets for Enhanced Photoelectric Detection and Photocatalytic CO₂ Reduction. *J. Phys. Chem. Lett.* **2019**, *10*, 6590–6597. [[CrossRef](#)] [[PubMed](#)]
32. Bharti, B.; Kumar, S.; Lee, H.; Kumar, R. Formation of oxygen vacancies and Ti³⁺ state in TiO₂ thin film and enhanced optical properties by air plasma treatment. *Sci. Rep.* **2016**, *6*, 32355. [[CrossRef](#)]
33. Shao, Y.; Gao, W.; Yan, H.; Li, R.; Abdelwahab, I.; Chi, X.; Rogée, L.; Zhuang, L.; Fu, W.; Lau, S.P.; et al. Unlocking surface octahedral tilt in two-dimensional Ruddlesden-Popper perovskites. *Nat. Commun.* **2022**, *13*, 27747. [[CrossRef](#)] [[PubMed](#)]
34. Regulacio, M.D.; Han, M. Multinary I-III-VI₂ and I₂-II-IV-VI₄ Semiconductor Nanostructures for Photocatalytic Applications. *Acc. Chem. Res.* **2016**, *49*, 511–519. [[CrossRef](#)]
35. Zhang, Z.; Yates, J.T. Band Bending in Semiconductors: Chemical and Physical Consequences at Surfaces and Interfaces. *Chem. Rev.* **2012**, *112*, 5520–5551. [[CrossRef](#)] [[PubMed](#)]
36. Wang, L.; Zhao, X.; Lv, D.; Liu, C.; Lai, W.; Sun, C.; Su, Z.; Xu, X.; Hao, W.; Dou, S.X.; et al. Promoted Photocharge Separation in 2D Lateral Epitaxial Heterostructure for Visible-Light-Driven CO₂ Photoreduction. *Adv. Mater.* **2020**, *32*, 2004311. [[CrossRef](#)]
37. Huang, H.; Li, X.; Wang, J.; Dong, F.; Chu, P.K.; Zhang, T.; Zhang, Y. Anionic Group Self-Doping as a Promising Strategy: Band-Gap Engineering and Multi-Functional Applications of High-Performance CO₃²⁻-Doped Bi₂O₂CO₃. *ACS Catal.* **2015**, *5*, 4094–4103. [[CrossRef](#)]
38. Huang, H.; Tu, S.; Zeng, C.; Zhang, T.; Reshak, A.H.; Zhang, Y. Macroscopic Polarization Enhancement Promoting Photo- and Piezoelectric-Induced Charge Separation and Molecular Oxygen Activation. *Angew. Chem. Int. Ed.* **2017**, *56*, 11860–11864. [[CrossRef](#)]
39. Li, Y.; Ouyang, S.; Xu, H.; Wang, X.; Bi, Y.; Zhang, Y.; Ye, J. Constructing Solid-Gas-Interfacial Fenton Reaction over Alkalinized-C₃N₄ Photocatalyst to Achieve Apparent Quantum Yield of 49% at 420 nm. *J. Am. Chem. Soc.* **2016**, *138*, 13289–13297. [[CrossRef](#)]
40. Zhang, H.; Wu, Q.; Guo, C.; Wu, Y.; Wu, T. Photocatalytic Selective Oxidation of 5-Hydroxymethylfurfural to 2,5-Diformylfuran over Nb₂O₅ under Visible Light. *ACS Sustain. Chem. Eng.* **2017**, *5*, 3517–3523. [[CrossRef](#)]
41. Krivtsov, I.; García-López, E.I.; Marci, G.; Palmisano, L.; Amghouz, Z.; García, J.R.; Ordóñez, S.; Díaz, E. Selective photocatalytic oxidation of 5-hydroxymethyl-2-furfural to 2,5-furandicarboxyaldehyde in aqueous suspension of g-C₃N₄. *Appl. Catal. B* **2017**, *204*, 430–439. [[CrossRef](#)]
42. Su, F.; Mathew, S.C.; Lipner, G.; Fu, X.; Antonietti, M.; Blechert, S.; Wang, X. mpg-C₃N₄-Catalyzed Selective Oxidation of Alcohols Using O₂ and Visible Light. *J. Am. Chem. Soc.* **2010**, *132*, 16299–16301. [[CrossRef](#)] [[PubMed](#)]
43. Duan, Y.; Wang, R.; Liu, Q.; Qin, X.; Li, Z. Tungsten Promoted Ni/Al₂O₃ as a Noble-Metal-Free Catalyst for the Conversion of 5-Hydroxymethylfurfural to 1-Hydroxy-2,5-Hexanedione. *Front Chem.* **2022**, *10*, 857199. [[CrossRef](#)] [[PubMed](#)]
44. Braun, J.V.; Blessing, G.; Zobel, F. Katalytische Hydrierungen unter Druck bei Gegenwart von Nickelsalzen, VI.: Nitrile. *Chem. Ges.* **1923**, *56*, 1988–2001. [[CrossRef](#)]
45. Huang, L.; Li, D.; Liu, J.; Yang, L.; Dai, C.; Ren, N.; Feng, Y. Enhanced mass transfer and service time of mesh Ti/Sb-SnO(2) electrode for electro-catalytic oxidation of phenol. *Environ. Sci. Pollut. Res. Int.* **2020**, *27*, 42072–42081. [[CrossRef](#)] [[PubMed](#)]
46. Cao, X.; Chen, Z.; Lin, R.; Cheong, W.; Liu, S.; Zhang, J.; Peng, Q.; Chen, C.; Han, T.; Tong, X.; et al. A photochromic composite with enhanced carrier separation for the photocatalytic activation of benzylic C-H bonds in toluene. *Nat. Catal.* **2018**, *1*, 704–710. [[CrossRef](#)]
47. Ye, L.; Han, Y.; Xi, J.; Wang, X.; Lu, X. Differences of Short Straight-Chain Monoalcohols in the Value-Added Conversion of Furfural Catalyzed by Zr₃AlI-MMO: Effect of Hydroxyl Position and Carbochain Length. *ACS Sustain. Chem. Eng.* **2021**, *9*, 13312–13323. [[CrossRef](#)]

Disclaimer/Publisher's Note: The statements, opinions and data contained in all publications are solely those of the individual author(s) and contributor(s) and not of MDPI and/or the editor(s). MDPI and/or the editor(s) disclaim responsibility for any injury to people or property resulting from any ideas, methods, instructions or products referred to in the content.